

Nanoscale ultrasonic subsurface imaging with atomic force microscopy

Cite as: J. Appl. Phys. **128**, 180901 (2020); doi: [10.1063/5.0019042](https://doi.org/10.1063/5.0019042)

Submitted: 22 June 2020 · Accepted: 22 October 2020 ·

Published Online: 9 November 2020



Chengfu Ma^{1,a)}  and Walter Arnold^{2,b)} 

AFFILIATIONS

¹CAS Key Laboratory of Mechanical Behavior and Design of Materials, Department of Precision Machinery and Precision Instrumentation, University of Science and Technology of China, Hefei 230026, China

²Department of Materials Science and Engineering, Saarland University, D-66123 Saarbrücken, Germany

^{a)}Electronic mail: chfuma@ustc.edu.cn

^{b)}Author to whom correspondence should be addressed: w.arnold@mx.uni-saarland.de

ABSTRACT

Imaging of subsurface features down to the nanometer scale is of great importance in various fields such as microelectronics, materials science, nanobiology, and nanomedicine. Since their invention 25 years ago, ultrasonic-based atomic force microscopy (AFM) techniques have attracted vast attention for their mechanical surface and subsurface sensing capability. In this Perspective article, we review the research on ultrasonic AFMs for subsurface imaging. We first describe the instrumentation setups and different detection schemes of ultrasonic AFMs. Then, attention is paid to the studies of the physical contrast mechanism, the evaluation of the detection capabilities, in particular, the detection depth limits, and the optimization approaches to enhance the contrast and to improve the detection depth. After that we present typical applications of using ultrasonic AFMs for detecting subsurface defects including dislocations, voids, and interfaces in functional materials and devices; visualizing embedded inclusions in composites; and imaging subcellular structures in biological materials. We conclude with an outlook of the challenges faced by ultrasonic AFMs toward fast, high resolution, and quantitative subsurface imaging.

Published under license by AIP Publishing. <https://doi.org/10.1063/5.0019042>

I. INTRODUCTION

Subsurface imaging techniques with nanoscale resolution are becoming increasingly important. This originates from the increasing demands and challenges for detecting subsurface defects in micro/nano electronic devices,¹ for inspecting embedded nanofilaments in composites, and for monitoring subcellular phenomena in bioscience.² In principle, subsurface objects such as voids, interfaces and embedded structures are detected due to their corresponding heterogeneous characteristics relative to the host material, inducing perturbations to the penetrating waves or fields employed for inspections. Such waves and fields can be based on optical, electrical, or acoustical techniques. Conventional noninvasive optical methods are not applicable for subsurface imaging of opaque materials. In addition, their resolution is limited due to diffraction and hence lies in the sub-micrometer scale. High resolution techniques such as scanning or transmission electron microscopy are not only very costly but also require extensive sample preparations in order

to image subsurface features. Many of these issues are discussed in Ref. 3.

Besides, ultrasound techniques are widely used in subsurface imaging and are the base for many quantitative non-destructive testing techniques. For instance, scanning acoustic microscopy (SAM)⁴ is routinely applied in the semiconductor industry for detecting voids, cracks, and delaminations within microelectronic devices. The spatial resolution of an SAM is limited by the Rayleigh criterion. Thus, applying ultrasonic waves with higher frequencies improves the resolution. Unfortunately, there is also a practical restriction for employing sub-micrometer wavelengths because of the losses in the acoustic lens, here in the coupling medium, usually water. Its attenuation increases with the frequency squared: $\alpha/f^2 \approx 2.2 \times 10^{-17} \text{ s}^2/\text{mm}$.⁵ This yields a return loss of $\approx 2 \times 19 \text{ dB}$ for a 1 GHz lens with a focal length of 100 μm , in addition to scattering within the component to be tested, and acoustic mismatch losses. Therefore, commercial SAMs are generally

operated at frequencies between 10 and 100 MHz.⁶ This frequency range also allows penetration into materials and provides a spatial resolution of some 10 μm to a few μm , which is not sufficient for detecting nanoscale defects.

The diffraction limit of acoustic microscopy may be overcome by using the concept of “near-field imaging.” In near-field acoustic microscopy, one uses an aperture or a tip as an antenna, which is brought into close proximity to the sample. Then, the spatial resolution is determined by the size of the antenna contacting the sample. Dürr *et al.*⁷ combined an aperture with an acoustic lens to obtain a super-resolution of $\lambda/4$. Khuri-Yakub *et al.* used a similar design.⁸ A scanning near-field acoustic microscope was built by Zieniuk and Latuszek⁹ using a pin probe as the antenna. The resolution is given by the diameter of the contacting pin, which is close to 10 μm .

A further step toward higher resolution for near-field acoustic imaging became possible with the invention of scanning probe microscopy (SPM) techniques. Considering the nanoscale probe tip in SPM, which has a typical size around 10 nm or even smaller, it was natural to combine SPM with ultrasound to realize nanoscale near-field acoustical imaging. Indeed, Takata *et al.*,¹⁰ Uozumi and Yamamuro,¹¹ Khuri-Yakub *et al.*,¹² Moreau and Ketterson¹³ presented acoustic imaging instruments based on scanning tunneling microscopy (STM). Either the sample was insonified monitoring its surface displacement by exploiting the exponential distance dependence of the tunneling current or by the ultrasonic transmission through tips. The amplitude of the acoustic signals was used for feedback to maintain the tip-sample spacing constant during scanning. The contrast was caused by changes in conductivity and topography, which cannot be easily separated. Chilla *et al.* used ultrasonic STM to detect the out-of-plane as well as the in-plane components of surface acoustic waves.¹⁴

While STM can only be applied on conductive samples, atomic force microscopy (AFM) has no such limitation. Therefore, efforts were concentrated on realizing acoustic imaging with AFM. Almost simultaneously, several different methods of detecting ultrasonic vibrations with an AFM were proposed. Cretin and Stal^{15,16} developed the so-called scanning microdeformation microscopy (SMM) with a vibrating tip exciting deformation on the sample surface that was detected by a transducer beneath the sample. They demonstrated imaging of subsurface defects in a depth of 100 μm with a resolution of 10 μm , which corresponds to the diameter of the tip. Based on the nonlinearity of the tip-sample force-distance curve, Kolosov and Yamanaka¹⁷ proposed to detect ultrasonic vibrations of the sample at frequencies much higher than the AFM cantilever resonances. Later, the group used an ultrasonic force microscope (UFM) for imaging subsurface defects in graphite with a resolution better than 10 nm.^{18,19} Rabe and Arnold^{20,21} added an optical knife-edge detector for an AFM to monitor ultrasonic surface vibrations with a bandwidth in the MHz range. Ultrasonic imaging with atomic resolution was also realized with their setup.²²

Since then, quite a number of related techniques have been developed, based on different excitation/detection schemes of ultrasonic vibrations. For instance, Rabe *et al.*²³ and Yamanaka *et al.*²⁴ respectively, developed atomic force acoustic microscopy (AFAM) and ultrasonic atomic force microscopy (UAFM) based on their earlier setups. In order to improve the detection sensitivity, both

AFAM and UAFM were operated at the resonance frequencies of the cantilever in contact with a sample. Thus, they are also referred to as contact-resonance AFM (CR-AFM).^{25,26} The use of much higher ultrasonic frequencies than the cutoff frequency of the detection photodiodes in AFMs became possible by employing heterodyne or amplitude demodulation techniques.^{14,27,28} The heterodyne force microscopy (HFM) is also called scanning near-field ultrasound holography (SNFUH).²⁹

The subsurface imaging potential of such ultrasonic AFM techniques have been shown on well-prepared model samples with embedded inclusions,^{29–32} voids,^{33–37} or other structures.^{38–40} The detection of defects in highly oriented pyrolytic graphite (HOPG) samples,^{41–43} internal voids in integrated circuits,^{29,44} adhesive interfaces,²⁵ and subcellular structures^{29,45,46} was also demonstrated. Besides, ultrasonic AFMs were too used for surface mechanical mapping of materials,^{47–53} based on the sensitivity of the cantilever resonance to contact stiffness. In particular, by employing proper contact-resonance models^{26,54–58} with the appropriate cantilever vibration and tip-sample contact models, quantitative measurement of the elastic^{59–61} and viscoelastic^{62–64} properties could be achieved.

In this Perspective article, we concentrate on the state of the art of subsurface imaging, using ultrasonic AFMs. To this end, we first present the development and working principles of multiple operating schemes of ultrasonic AFMs. Next, we discuss the studies on the physical contrast mechanism of ultrasonic AFMs for subsurface imaging, followed by efforts toward the evaluation and the optimization of the detection capability. Finally, we conclude with a discussion of the challenges and potential application opportunities facing ultrasonic AFMs.

II. INSTRUMENTATION AND IMAGING SCHEMES

As mentioned earlier, a number of ultrasonic AFM techniques have been proposed based on different excitation and detection schemes for ultrasonic waves. They are called AFAM, UAFM, and HFM. Their operation principles are shown schematically in Fig. 1. In general, ultrasonic AFMs are realized in the contact mode. They have in common that the cantilever is excited into oscillations. Their theoretical descriptions are based on the same differential equation but with different boundary conditions.

In the AFAM technique,⁵⁶ the ultrasonic waves are generated by an external transducer, which is inserted between the AFM scanner and the sample. A coupling medium such as honey is used to bond the sample onto the transducer. Typically, the transducer has a center frequency of some MHz and generates longitudinal ultrasonic waves with the frequency f_1 supplied by a function generator. The ultrasonic waves transmit through the sample and cause out-of-plane vibrations of the sample surface. The surface displacements force the AFM cantilever to oscillate through the contacting tip. By recording the cantilever deflections with the photodiode and analyzing the signal with a lock-in amplifier, amplitude and phase of the cantilever vibration are extracted. Since the ultrasonic vibration frequency is much higher than the frequency of the feedback loop, scanning of the topography in the contact mode is not affected. Therefore, acoustic amplitude and phase images are

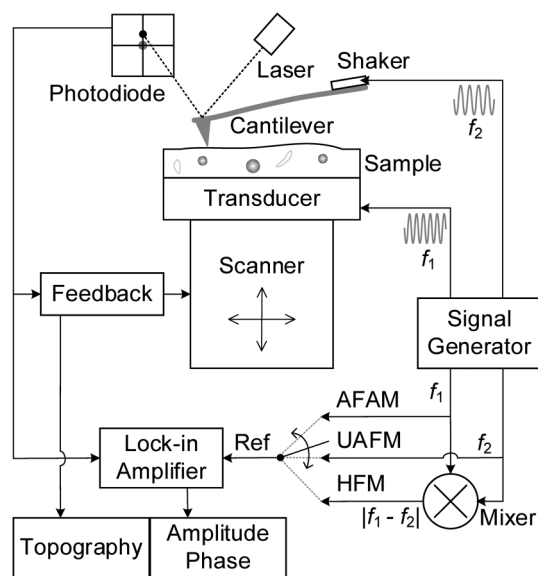


FIG. 1. Principle setups for ultrasonic AFMs with three different excitation/detection schemes: AFAM, UAFM, and HFM.

simultaneously obtained, together with the topography, at a regular contact-AFM rate.

In order to excite the cantilever oscillations, one employs in UAFM the built-in piezo-shaker directly in the cantilever holder instead of an additional transducer (Fig. 1).⁶⁵ The piezo-shaker is normally used for tapping mode AFM. Therefore, UAFM is possible in most commercial AFMs without any modifications.

In order to improve the signal-to-noise ratio (SNR), qualitative amplitude and phase imaging in both AFAM and UAFM are carried out at the cantilever CR frequencies, which are typically in the range of over 10 kHz to 1 MHz. This requires the determination of the cantilever CRs before imaging. In addition, measurements of CR frequencies and quality factors are needed for quantitative elastic and viscoelastic characterizations.^{56,58} Sweeping the excitation frequency yields the resonance frequencies and quality factors of the cantilever's flexural CR modes. However, it is not practical to obtain CR frequency or quality factor maps by sweeping the spectra pixel-by-pixel, due to the relatively low acquisition rate. Therefore, such quantitative spectroscopy measurements are often carried out at a fixed single point. This problem has been addressed with resonance tracking electronics^{66–69} or by the band excitation method^{70,71} in which the cantilever is excited over a band of frequencies centered on a CR resonance simultaneously and the cantilever response is recorded and analyzed by fast Fourier transformation. Additionally, it should be mentioned that in the cantilever's oscillations, spurious resonance peaks^{72,73} are often seen, which are detrimental for determining the correct CRs. This also holds for cantilevers in liquids.⁷⁴ Magnetic,⁷⁵ photothermal,^{76,77} and Lorentz force⁷⁸ actuation methods can be employed to address this issue.

In HFM²⁸ and other analogs,^{29,30} ultrasonic waves are launched both from beneath the sample, like in AFAM, with a

frequency of f_1 and at the cantilever base with a frequency of f_2 as in UAFM (see Fig. 1). In HFM, the frequencies f_1 and f_2 are slightly different. The nonlinear interaction between the tip and the sample surface mixes the two ultrasonic waves and generates a heterodyne signal at the difference frequency $|f_1 - f_2|$. Since $|f_1 - f_2|$ is lower than the cutoff frequency of the AFM detection system, the resulting cantilever oscillation at $|f_1 - f_2|$ is then detected by the photodiode. The amplitude and phase are monitored with a lock-in amplifier by using an external reference signal $|f_1 - f_2|$. If there is a change of the phase difference $\Delta\phi$ between the two signals, caused by interaction of the tip with the sample, the phase shift is enhanced by the factor $|f_1/(f_2 - f_1)|$. This effect of heterodyning is well-known in rf-technology and has been exploited for precise ultrasonic sound velocity measurements in the GHz range.⁷⁹ To enhance the SNR, the frequency difference $|f_1 - f_2|$ in HFM is usually tuned to one of the CRs of the AFM cantilever.

III. CONTRAST MECHANISM

A. Two viewpoints

The origin of the contrast in ultrasonic AFM images was and still is a matter of debate and controversy. A clear analysis is mainly hindered by the complexity that the image contrast not only involves wave propagation in the sample but also the tip-sample interaction as well as the different signal detection schemes. There are two viewpoints with regard to the contrast mechanism. The first one attributes the contrast origin to the scattering of the ultrasonic waves by the subsurface feature.^{29,38,80} As conceptually illustrated in Fig. 2(a), the incident ultrasonic wave propagates through the sample and is collected at the sample surface by the AFM tip as an antenna. If there is an embedded feature in the host material, such as an inclusion or a void, scattering of the ultrasonic wave occurs and the ultrasonic wave field between the feature and the surface is perturbed. Thus, by monitoring the perturbations by the cantilever tip, the subsurface feature is imaged. In the second viewpoint, the subsurface contrast originates from variations of the

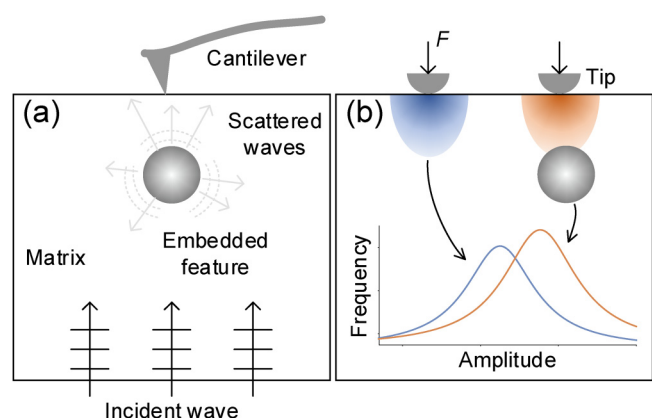


FIG. 2. Possible contrast mechanisms for subsurface imaging using ultrasonic AFMs. (a) Scattering of the incident ultrasonic waves by the embedded object; (b) contact stiffness/damping variations induced at the surface by the subsurface object.

contact stiffness or the damping induced by the buried object in the host material.^{25,31,34,39,41,43,81–83} As can be seen in Fig. 2(b), when the AFM tip is brought into contact with the sample surface, a stress field is generated by the indenting tip, which extends into the sample subsurface. If the stress field extends deep enough to the location of a mechanically heterogeneous structure, the contact stiffness or the damping is altered, which is then sensed by the tip. This subsequently shifts the CR of the cantilever [see the inset in Fig. 2(b)], and the existence of the subsurface structure can thus be discerned from the vibration signals of the cantilever.

B. Contact stiffness

Quite a lot of efforts have been devoted to clarify the subsurface contrast mechanism of ultrasonic AFMs. For example, Yaralioglu *et al.*⁸⁴ proposed an approach to calculate the contact stiffness between a layered material and an AFM tip based on the surface impedance method. In this way, Sarioglu *et al.*⁸⁵ modeled the effect of subsurface interface defects on the local contact stiffness and investigated analytically the sensitivity of UAFM for such defects. Their result was supported by experiments carried out by Hurley *et al.*,²⁵ where AFAM was employed to image inhomogeneous adhesion areas between a substrate and adhered films (Si/Au and Si/Ti/Au).

Consistent with theory, the images reveal a decrease of 4%–5% in contact stiffness for the poor adhesion areas. In additional work by Parlak and Degertekin,³³ three-dimensional (3D) finite element analysis (FEA) was used to simulate the contact stiffness sensed by an AFM tip above a sample including buried features. By performing AFAM experiments on samples with well-defined subsurface cavity structures, the authors showed that their 3D FEA model is in good agreement with the AFAM contact stiffness measurements. These efforts demonstrate that subsurface features can be revealed by quantitative measurements of contact stiffness variations in CR-AFMs, both in the AFAM and UAFM modes.

Furthermore, Ma *et al.*⁸⁶ verified contact stiffness variations as the key contrast mechanism in CR-AFM subsurface imaging. Simulations based on such a mechanism were applied for the contrast, as shown in Fig. 3. For example, Figs. 3(a) and 3(b) show, respectively, the topography and AFAM amplitude image of a 125 nm thick highly oriented pyrolytic graphite (HOPG) flake positioned on a Si substrate containing patterns of nine open holes with diameters from 1927 nm to 178 nm. Scanning was made with a tip load of 293 nN with a Multi75-G cantilever having a calibrated spring constant of 3.1 N/m. The working frequency of 350 kHz was close to the CR. It can be seen from Fig. 3(b) that the covered cavity features are clearly revealed in the AFAM amplitude image.

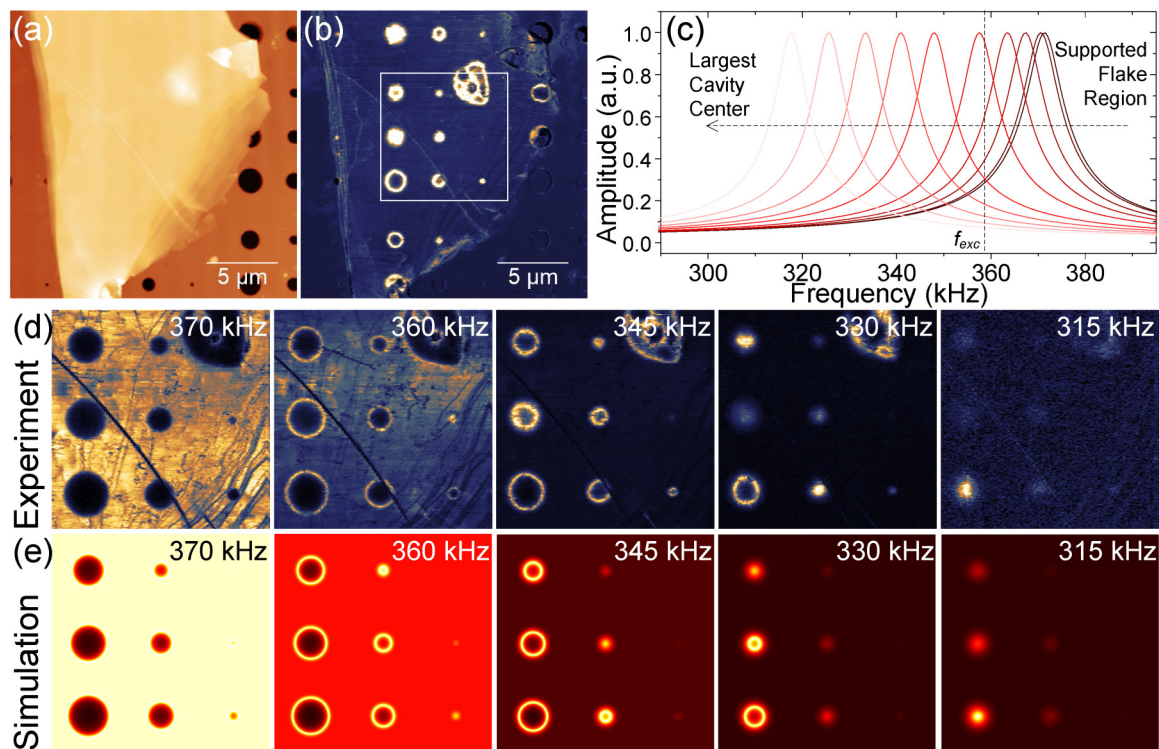


FIG. 3. (a) Topography and (b) AFAM amplitude image on a HOPG flake with a thickness of 125 nm; (c) simulated CR spectra on the HOPG flake obtained, respectively, at the supported region and at the centers of the nine subsurface cavities indicated by the encased area in (b); (d) AFAM amplitude images of the encased area in (b) taken at five frequencies; (e) simulated amplitude images for the frequencies used for (d). Reproduced with permission from Ma *et al.*, J. Appl. Phys. **126**, 124302 (2019). Copyright 2019 AIP Publishing LLC.

However, they are not visible in the topography image. The amplitude and phase contrast in AFAM and UAFM are qualitative because they are determined by the imaging parameters, for instance, by the working frequency as shown in Fig. 3(d). It shows amplitude images of the nine covered cavities in the encased area in Fig. 3(b) for various excitation frequencies. Except for the smallest cavities, which are indistinguishable due to the topography related feature in the upper right corner, the remaining cavities are all visible. However, their contrasts change and even reverse with varying the excitation frequency. Moreover, it can be seen that by decreasing the excitation frequency, bright halo features appear at the cavity peripheries which contract toward the cavity centers with decreasing frequency. The observations can be explained by considering that the subsurface cavity structures induce contact stiffness variations which depend on their diameters and the scanning position entailing CR shifts of the cantilever across the scan area. Therefore, by employing different excitation frequencies for imaging, bright contrasts appear at positions where the CR frequency coincides with the excitation frequency. More quantitatively, the contrast observed in Fig. 3(d) was simulated based on the above mechanism. To do so, a contact stiffness map was built considering a Hertzian contact model for the tip-sample pair, as well as an edge-clamped circular freestanding plate model for the cavities. Then, a CR frequency map was calculated according to the dispersion curve of the cantilever obtained from a proper CR model.⁵⁶ Furthermore, the amplitude response of the cantilever was calculated by describing the cantilever as a driven damped harmonic oscillator. Typical CR spectra on the supported flake region and above the centers of the nine cavities are shown in Fig. 3(c). A quality factor of $Q = 50$ was used based on experimental data. From the CR spectrum map, the amplitude image can be obtained for a specific excitation frequency f_{exc} . Figure 3(e) shows the simulated amplitude images for the scan area in Fig. 3(d) with the same setup parameters. It can be seen that the experimentally observed contrasts are simulated quite precisely. This strongly supports that the contact stiffness is the key contrast mechanism for subsurface imaging in AFAM and UAFM.

At a depth of $3a_c$, the stress-field amplitude of the tip is approximately ten times smaller than its amplitude at the surface.⁸⁷ As a rule of thumb, such a depth is, therefore, considered to define the detection depth limit based on AFM stiffness sensing. In Hertzian contact mechanics, $a_c = (3RF_N/4E^*)^{1/3}$, where R is the tip radius, F_N is the applied tip load and $E^* = ((1 - \nu_t^2)/E_t + (1 - \nu_s^2)/E_s)^{-1}$ is the reduced indentation modulus of the tip and sample with (E_t, ν_t) and (E_s, ν_s) being, respectively, their Young's modulus and Poisson's ratio. For typical values of $E^* = 50$ GPa, $F_N = 100$ nN, and $R = 100$ nm, this yields $3a_c \approx 16$ nm.

However, such a simple rule of thumb does not explain the observed detection depths in some ultrasonic AFM experiments. This is especially true when imaging of subsurface structures deeply embedded in soft materials was reported by using HFM, for example, the 15 nm diameter Au nanoparticles buried under a 500 nm thick polymer film.²⁹

C. Ultrasonic scattering

In order to explain the experimentally observed detection depth, scattering by subsurface features of the ultrasonic wave

propagating through the sample is considered usually. Since ultrasound with frequencies of a few MHz are often used in HFM, their wavelengths in the specimens are of the order of a few millimeter, which is much larger than the nanoscale subsurface objects. Rayleigh scattering by the embedded nanostructures is expected. In the Rayleigh regime, the total scattering cross-section σ scales as the sixth power of the scatterer size, here the radius a in the case of a nanoparticle, and varies inversely with the fourth power of the wavelength λ .⁸⁸ By normalizing σ with the geometrical cross-section πa^2 of the particle, the efficiency of scattering can be estimated by the factor σ_N ,

$$\sigma_N = \frac{\sigma}{\pi a^2} = \frac{4\pi}{9} g_e k_1^4 a^6 / \pi a^2 = \frac{4}{9} g_e (k_1 a)^4, \quad (1)$$

where $k_1 = 2\pi/\lambda$ is the longitudinal wavenumber and g_e is a parameter determined by the Lamé's constants and the density of both the host and the particle materials.^{88,89} For the practical case of a gold particle in a polymer matrix, $g_e \approx 3 \times 10^3$. This entails $\sigma_N \approx 10^{-10}$ for a particle radius of $a = 50$ nm and an ultrasonic wavelength of $\lambda \approx 0.5$ mm in a polymer with a velocity of $v_L = 2.3$ mm/ μ s. For rigid spherical particles one gets similar values. For voids in a polymer, the contrast is further reduced by a factor of 100 and for a gold particle in water by a factor of 10^3 . For the relative scattered intensity at the surface center above the buried nanoparticle $I_s/I_0 \approx g_e k_1^4 a^6 / r^2$ holds,⁹⁰ where r is its depth. Note that the forward scattered field at the surface decreases as r^2 . This means that the forward scattered amplitude signal is $\approx 10^{-6}$ below the transmitted signal for $r = 250$ nm, which is hardly detectable by even the most advanced ultrasonic nondestructive testing system. These numbers are only the basis for further discussions, because the condition of plane waves is not fulfilled in a setup like in Fig. 2, and because of the multiple reflections in the sample, which must be taken into account.

Cantrell *et al.* were the first to model the HFM setup theoretically.³⁰ The difference frequency was set to a contact-resonance. They took into account different contributions to the total phase shift of the measured continuous wave signal caused (1) by the difference in elastic modulus relative to the host material of the buried nanostructures; (2) by the multiple reflected and transmitted signal; (3) by the frequency shift caused by the non-linear interaction in the mixing process (see above); and (4) by changes in the contact stiffness. For an experimental test, they examined a layer of randomly distributed gold particles of 10–15 nm diameter buried 7 μ m deep in a polyimide polymer. The expected theoretical phase shift is about 1 mdeg, which is much smaller than the measured value of $\approx 2^\circ$. Therefore, Cantrell *et al.* suggested that the gold particles altered the surrounding material, being responsible for the large shift.

Verbiest *et al.*⁸⁰ undertook analytical and FEA calculations for scattering at a gold particle embedded 200 nm deep in poly(methyl methacrylate) (PMMA). In the analytical model, the interference between the incoming and the scattered waves above the particle was taken into account. In the FEA model, multiple reflections at the walls of the sample were additionally considered. Both effects led to an increase in the amplitude contrast, here 10^{-4} . The phase contrast turned out to be a few mdeg, which is still an order of

magnitude below the detection limit of ≈ 20 mdeg for an AFM. Furthermore, Verbiest *et al.* also found that the expected size of the particle in the phase image is significantly larger than its geometrical size, similar to the findings of Cantrell *et al.*³⁰ This contradicts with reported experiments, where no obvious enlargement of the features in the contrast was observed.^{29,45} In a subsequent paper, Verbiest *et al.*⁹¹ attributed the contrast mechanism to frictional dissipation of the oscillating nanoparticles after ruling out other possibilities, in particular, ultrasonic scattering. The mechanism of elasticity variations was excluded since calculations of the cantilever dynamics of HFM⁹² did not support the observed contrasts. The frictional entails an imaginary contribution to the contact stiffness.

Sharahi *et al.*⁹³ applied the model of Cantrell *et al.*³⁰ to the case of a buried cavity, taking scattering additionally into account. The cavity with a radius of 200 nm was located 500 nm deep in a polymer material. By estimating the phase contrast in the heterodyne signal due to the local contact stiffness variation as well as scattering, they concluded that the contrast in the HFM phase image depends on both.

It is difficult to compare the experimental data of Sharahi *et al.*,⁹³ Cantrell *et al.*,³⁰ and of Verbiest *et al.*⁹¹ with each other, because the radii and the depths of the particles are different. Even small increases in defect size a can lead to a signal just above noise, see Eq. (1). Finally, the $1/r^2$ depth dependence was indeed observed in SMM.¹⁶

Kimura and co-workers³² carried out comprehensive experimental studies in order to clarify whether different excitation/detection schemes determine the subsurface imaging contrast in ultrasonic AFM. In their experiments, they investigated HFM, AFAM, 2nd-harmonic AFAM, and force modulation microscopy (FMM) for sub-surface imaging on model samples of Au nanoparticles buried in polymer bulk materials. FMM is a widely used contact-AFM imaging mode for surface mechanical property measurements, where the tip-sample interaction is mechanically modulated and analyzed at a frequency far below the resonance.^{94,95} In FMM, the cantilever dynamic response is analyzed at the same frequency as the excitation one. AFAM at the 2nd-harmonic was used by Kimura *et al.* in order to investigate the nonlinear interaction in which the sample is excited at half the CR frequency $f_{CR}/2$ and detected at f_{CR} . The results showed that detection at the difference frequency in HFM or at the 2nd-harmonic frequency caused by nonlinear tip-sample interaction, is not essential for imaging subsurface nanoparticles. This was concluded from the fact that one can also visualize nanoparticles buried in a depth of almost $1\mu\text{m}$ with AFAM, besides HFM and 2nd-harmonic AFAM. For example, Figs. 4(a)–4(c) show, respectively, the topography, the AFAM amplitude and the HFM amplitude images of Au particles buried under a 900 nm thick photopolymer film. Here, a cantilever with a spring constant of 1.3 N/m was used. Except for the small drift of the HFM image, it can be seen that AFAM reveals the

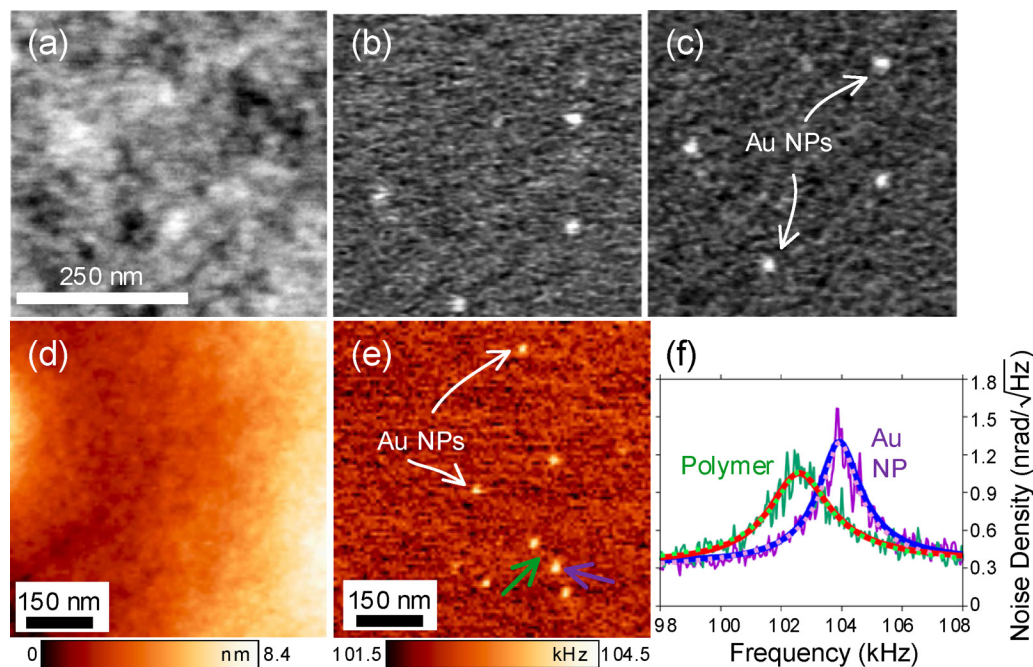


FIG. 4. (a) Topography and (b) AFAM amplitude image of Au nanoparticles (NPs) of 50 nm diameter buried under a 900 nm thick photopolymer film; (c) HFM amplitude image of the particles in (b) with a small scanning drift; (d) topography and (e) CR frequency map of Au nanoparticles buried 300 nm below a photopolymer film obtained with STNM; (f) The thermal noise spectra recorded at the locations indicated by the arrows shown in (e). (a)–(c) Reproduced with permission from Kimura *et al.*, *Ultramicroscopy* **133**, 41 (2013). Copyright 2013 Elsevier B.V. (d)–(e) Reproduced from Yao *et al.*, *Sci. Rep.* **7**, 42718 (2017). Copyright 2017 Author(s), licensed under a Creative Commons Attribution (CC BY) License.

nanoparticles with a contrast as good as the HFM. In addition, the authors showed that detection at the CR is playing a major role for resolving the subsurface nanoparticles, since unlike the other three methods which detect the oscillatory signal at the CR, FMM failed in imaging nanoparticles under a 200 nm thick cover. Due to these experimental results, Kimura *et al.* suggested that the subsurface features become visible because they affect the local viscoelasticity and, therefore, modify the CR, i.e., its frequency and Q -factor. This idea was further verified by using resonance tracking AFAM and CR spectroscopy to quantitatively measure the CR frequency and Q -factor.⁹⁶ There is a higher CR frequency and a higher Q -factor at the surface centers of the subsurface particles as compared with the surrounding area. This suggests that the embedded Au nanoparticle in the soft host material induces higher contact stiffness and lower local damping, i.e., also modifies the imaginary part of the contact stiffness.

Soon the question arose whether one really needs to exploit ultrasonic excitations to detect subsurface features if the contrast originates from changes of the local contact stiffness and damping. This motivated Yao *et al.*⁹⁷ to use scanning thermal noise microscopy (STNM) to further verify such a mechanism by excluding ultrasonic effects. In STNM, the cantilever deflection was recorded at each pixel while scanning the tip across the surface in contact-AFM mode. Then, using a fast Fourier transform algorithm, the thermal noise spectrum was analyzed, yielding maps of the CR frequency and the Q -factor by fitting the spectra. In this way, Yao *et al.* demonstrated the visualization of Au nanoparticles with diameters of 40 nm buried under a 300 nm thick photopolymer film, see Fig. 4(e). It can be seen that the nanoparticles are clearly revealed by the STNM CR frequency map. However they are not visible in the topography image [Fig. 4(d)]. Comparing the recorded thermal noise spectra at the surface center of a nanoparticle with the one at its surrounding area, as shown in Fig. 4(f), a shift of the CR to a higher frequency, induced by the subsurface nanoparticle, can be observed. A further analysis revealed an increase of 15% of the contact stiffness and a decrease of 16% of the local damping, due to the presence of the Au nanoparticles in the host material.

Although it is still not clear why nanoparticles in such deep depths influence the local stiffness and damping on the surface center, the experimental studies make us confident that the contact stiffness differences due to elasticity and damping variations relative to the host material induced by subsurface features, are the key contrast mechanism for subsurface imaging in ultrasonic AFMs using mm wavelengths.

D. Subsurface imaging using GHz ultrasound

In order to detect buried defects with an ultrasonic AFM at depths where they no longer exert a measurable influence on the contact stiffness, much higher frequencies must be used for scattering determining the contrast. From Eq. (1), it is evident that $k_1 a$ should be made as large as possible, i.e., wavelengths $\lambda \approx$ defect size a . This calls for GHz ultrasonic frequencies. In order to make this feasible, a different HFM technique to image subsurface structures was proposed by Hu *et al.*³⁸ Line structures made of gold with 1.5 μm width and 100 nm thickness, covered by a 7 μm thick

photo-resist layer, were insonified with 1 GHz ultrasonic waves (wavelength some μm), which were amplitude modulated at a fraction or at a multiple frequency of a cantilever contact-resonance. The transmitted signals were demodulated by the nonlinear tip-surface interaction in an analog way to rf-am demodulation. Defects in the devices were imaged based on the contrast due to ultrasonic scattering and transmission differences, which were determined by the acoustic mismatch between the elastic properties of the host material and the defects, by their geometry, and by diffraction effects when traversing the buried structures. The difference to the other HFM schemes lies in the fact that wavelengths three orders of magnitudes smaller were used.

The GHz ultrasonic AFM setup by Hu *et al.*³⁸ was also used by Büchenschütz-Göbeler *et al.*⁹⁸ to investigate cells in order to measure their elastic properties. In the experimental setup, as shown in Fig. 5(a), a live-cell sample was insonified through its bottom by a GHz transducer, which was excited by an amplitude-modulated signal having a carrier frequency f_c of 1 GHz order and a modulation frequency f_m equal to the cantilever's first mode contact-resonance frequency (≈ 40 kHz). The nonlinear tip-sample interaction demodulated the transmitted signal, enabling one to pickup its amplitude and phase signals from the AFM cantilever's oscillation response,³⁸ together with the topography imaging. Figure 5(b) shows the imaging results obtained on type II Madin-Darby Canine Kidney (MDCK) cells using a carrier frequency of 1.15 GHz. The topography image shows a cluster of elongated cells which have widths of about 10 μm . In the amplitude image, one can see fringes surrounding the cell centers. This indicates interference originating from ultrasonic scattering at the cell nucleus with a size of some μm which is comparable to the wavelength. To confirm this findings, theoretical calculations of the wave field scattered by the nucleus were carried out. The nucleus was modeled as a fluid sphere with a radius of 4 μm and a density of 1.4 g/cm³, while its surrounding medium was modeled as water. The sound velocities in the nucleus and in the medium were set, respectively, 1300 m/s and 1500 m/s. Figure 5(c) shows the resulting normalized pressure amplitude of the scattered waves. The calculated interference pattern agrees well with the observed pattern. This corroborates the contribution of ultrasonic scattering to the subsurface imaging contrast in GHz ultrasonic AFM.

This mechanism was further verified by van Es *et al.*⁹⁹ on silicon samples with grooves etched into the surface which were then covered by a 5 μm thick PMMA polymer. By employing different carrier frequencies, a distinct pattern change was observed on the surface of the PMMA, demonstrating that ultrasonic scattering at the subsurface grooves is the dominant contrast mechanism.

IV. DETECTION CAPABILITY AND ITS OPTIMIZATION

While the spatial resolution for an ultrasonic AFM is determined by the tip-sample contact area and is typically below 10 nm, the detection depth is determined by many factors. Investigations of the sensing depth of ultrasonic AFMs were performed experimentally on different test samples. For example, Crozier *et al.*¹⁰⁰ demonstrated the application of AFAM for thickness measurements of thin films. Their results show that AFAM allows to differentiate photoresist, tungsten, and copper films deposited on silicon

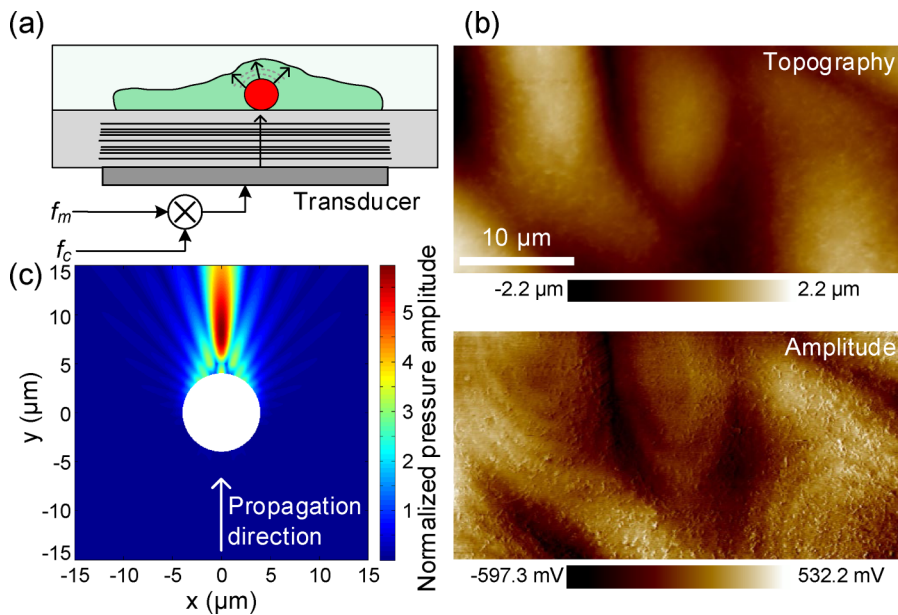


FIG. 5. (a) Schematic illustration showing the scattering of plane acoustic waves by the nucleus of a type II MDCK cell deposited on substrate of silicon nitride; (b) topography (upper) and amplitude (lower) images of the cells obtained with GHz ultrasonic AFM by using a carrier frequency of 1.15 GHz; (c) simulated scattered wave field in water (medium) by a fluid sphere (nucleus) showing the normalized pressure amplitude. Reproduced with permission from Büchenschütz-Göbel et al., *Verhandl. Deutsch. Phys. Gesellschaft, Spring Meeting (Regensburg, Germany, March 2013)*, BP 13.5. Copyright 2013, I. Phys. Institut, Georg-August-Universität Göttingen.

substrates up to thicknesses of, respectively, 300, 50, and 200 nm. The first, second, and fourth flexural eigenmodes of the cantilever were, respectively, used in the experiments in order to exploit their different modal sensitivities.^{101,102} The higher modes effectively stiffen the cantilever and hence allow deeper inspection. Other test samples comprised conically shaped cavities etched by focused ion beams in silicon substrates,^{33,36} buried holes with well-defined dimensions and depths,^{34,37,86} and metal structures covered under different depths of polymer layers.⁴⁰ Subsurface features at a depth of some hundred nanometers were shown to be detectable, depending on their dimensions, the material properties and the imaging parameters.

Analytical models of evaluating the detection capabilities are desirable. Based on the contact stiffness mechanism, a subsurface feature can only be distinguished from the host material if the induced contact stiffness difference Δk^* is larger than the stiffness sensitivity δk^* of the system. The stiffness sensitivity δk^* for a specific setup can be determined from the dispersion curves as shown in Fig. 6(a), which relate the CR frequency f_{CR} with the contact stiffness k^* . Here, f_{CR} and k^* are, respectively, normalized by the first free resonance frequency f_0 and the spring constant k_c of the cantilever. By knowing the minimal detectable CR frequency shift δf of the system, the corresponding minimal δk^* for a specific contact stiffness can be obtained for a given eigenmode. Then, the detectability of a subsurface feature can be determined by comparing Δk^* to δk^* . To do so, the contact mechanics between the tip and the sample containing the subsurface feature must be calculated. This is usually done with FEA modeling because with analytical models one can only describe simple cases. Figure 6(b) shows schematically the 3D FEA model used by Parlak and Degertekin³³ for calculating the contact stiffness for an AFM tip indenting a sample with subsurface defects. The FEA model simulates the contact stiffness profile while scanning the tip, here across a cylindrical cavity in a silicon substrate. The FEA model yielded contact

stiffness changes in good agreement with the experimental measurements. Based on the FEA model, one can predict whether a subsurface feature can be detected by comparing the maximal contact stiffness variation Δk^* induced by it to the threshold value δk^* . Considering a minimal detectable contact stiffness change of $\delta k^* = 10 \text{ N/m}$, Parlak and Degertekin calculated the maximal detectable depths for cylinders lying parallel to the surface in silicon substrates for various radii. Hollow cylinders, rigid cylinders, and cylinders consisting of silicondioxide and tungsten are considered. The resulting detection limit contours are shown in Fig. 6(c) from which one can read that subsurface features with a larger mechanical contrast compared to silicon can be detected more easily at larger depths. In addition, larger detection depths are found for larger structures, as expected. However, the slopes of the contour lines indicate that the detection depths for elastic and rigid cylindrical inclusions are limited to certain values, regardless of their sizes, unlike in case of the hollow cylinder.

For certain contact mechanic cases analytical models can be built. This applies for layered materials^{84,85} and subsurface cavities.^{35,86} For the latter, Ma *et al.*^{35,86} proposed an equivalent edge-clamped circular plate model for evaluating the detection limit for CR-AFM. To validate the effectiveness of the model, UAFM was applied to image subsurface cavities fabricated by using HOPG flakes of different thicknesses to cover a silicon substrate containing circular holes of various diameters.⁸⁶ An example of such images is shown in Figs. 7(a) and 7(b) which, respectively, show the topography and the UAFM amplitude image taken on a HOPG flake of a thickness of approx. 110 nm. For scanning, a Multi75-G cantilever was used with a spring constant of 3.1 N/m under an applied load of 210 nN. The working frequency was 410 kHz corresponding to the CR frequency of the first flexural mode on the silicon substrate. The UAFM amplitude image shows the covered cavities, except for the smallest. Furthermore, the detectability of the cavities was investigated for cover thicknesses of 25, 110, 247, and 392 nm. The

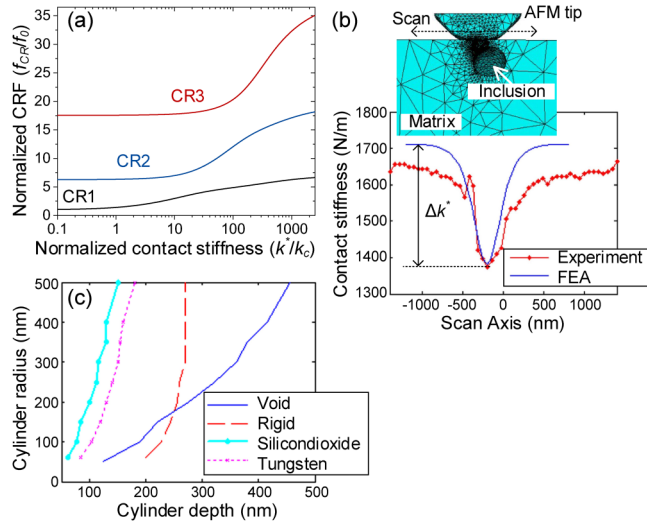


FIG. 6. (a) Relationships between the normalized CR frequency and the normalized contact stiffness for the first three flexural eigenmodes of a cantilever; (b) illustration of a 3D FEA model for simulating the contact between a scanning AFM tip and the host material containing a subsurface inclusion, and the experimentally measured and the calculated contact stiffness profiles across a subsurface cylindrical cavity with a radius of 465 nm and a depth of 85 nm in a silicon substrate; (c) detection limit contours for cylindrical objects of different materials in silicon substrates. Figures (b) and (c) are reproduced with the permission from Parlak *et al.*, J. Appl. Phys. **103**, 114910 (2008). Copyright 2008 AIP Publishing LLC.

results are displayed in Fig. 7(c) with the symbols “o” and “x” representing, respectively, the detected and undetected cavity features. As expected, with increasing depth, smaller cavities become gradually undetectable. Based on their model, Ma *et al.* calculated the contact stiffness at the surface centers of cavities for various diameters and depths where the contact stiffness deviates maximally from the substrate, as shown in Fig. 7(c). For their experiments, a contact stiffness sensitivity of $\delta k^* = 7 \text{ N/m}$ was determined, which yields a threshold contact stiffness of 289 N/m, considering a contact

stiffness of 296 N/m on the substrate. A contour line of 289 N/m then separates the undetectable from the detectable cavities in the map of Fig. 7(c). The experimental detectability of the cavities is in good agreement with the prediction of the model.

In order to improve the subsurface imaging contrast and the detection depth, the experimental parameters must be selected in such a way that one obtains maximal sensitivity for contact stiffness variations. For example, measurements should be performed at a CR frequency with the largest slopes of the dispersion curve of the employed mode. Figure 6(a) shows that the sensitivity of the CR frequency to the contact stiffness varies with the normalized contact stiffness k^*/k_c . For a Hertzian contact, k^* depends on the tip load F_N because $k^* = (6E^{*2}RF_N)^{1/3}$. Meanwhile, it can also be seen from Fig. 6(a) that different eigenmodes of the cantilever have different sensitivities, as a function of the contact stiffness.^{101,102} In addition, cantilevers with different spring constants show different sensitivity ranges for the contact stiffness.¹⁰³ Finally, the dispersion curve depends on the cantilever geometry, on the tip position, and on a number of other parameters.^{54,56,102,104} Summarizing this part, the tip load, the cantilever stiffness, and the eigenmode are the most effective and convenient parameters that can be selected to achieve high contact stiffness sensitivity. For imaging on a soft material (small contact stiffness), a soft cantilever and the first mode are the most sensitive to contact stiffness changes. However, for stiffer samples (large contact stiffness), a stiffer cantilever and higher modes become more sensitive.

Increasing the tip load leads to an increased tip-sample contact area and entails, at least in theory, a larger penetration depth of the stress field.⁸⁷ This effect was indeed observed,^{31,33,35,37,40} however, only in the range of small loads. A further increase did not help much in improving the contrast and the detection depth.^{31,35} Employing cantilevers with different spring constants is more effective for improving subsurface imaging.^{32,40} Finally, tuning the imaging contrast can also be achieved by using the cantilever's multiple eigenmodes. This can be explained by the different sensitivities of the various eigenmodes to contact stiffness changes,^{101,102} see Fig. 6(a). Figure 8 demonstrates CR images obtained by Ma *et al.*³⁵ The first three flexural modes of a cantilever were used to image in the UAFM mode subsurface cavities in a PMMA substrate covered by a HOPG flake with a thickness of approx. 102 nm. The averaged

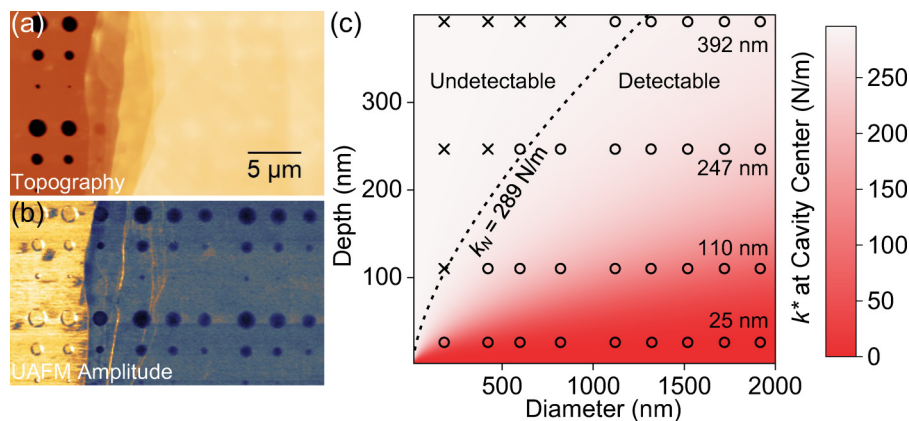


FIG. 7. (a) Topography and (b) UAFM amplitude image taken on a 110 nm thick HOPG flake covering a silicon substrate containing circular holes with various diameters; (c) Calculated contact stiffness k^* at the surface center of various diameters and depths. The dashed contour line in (c) separates the detectable cavities from the undetectable ones, the symbols “o” and “x” represent, respectively, the detected and undetected cavities in the experiments. Reproduced with the permission from Ma *et al.*, J. Appl. Phys. **126**, 124302 (2019). Copyright 2019 AIP Publishing LLC.

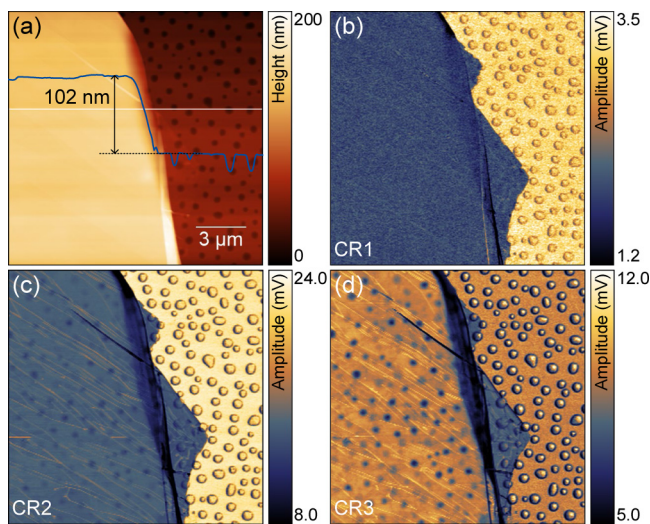


FIG. 8. (a) Topography image of a 102 nm thick HOPG flake positioned on a PMMA substrate containing holes with a mean diameter of approx. 503 nm, and (b)–(d) UAFM amplitude images obtained with the first three flexural modes. Reproduced with the permission from Ma *et al.*, J. Appl. Phys. **121**, 154301 (2017). Copyright 2017 AIP Publishing LLC.

diameter of the cavities was 503 nm. The cantilever's spring constant was 0.24 N/m and the operation frequencies were the first three CR resonance frequencies, i.e., 72.3, 213.9, and 440.2 kHz. Figure 8 shows that the image obtained with the first mode shows no subsurface cavities, which become, however, visible by the second mode with a blurry and by the third mode with a clear contrast. Hence, the detection depths are in these cases smaller, slightly larger, and eventually much larger than the flake thickness of 102 nm. This was confirmed by theoretical evaluation which yields detection depths of 51, 104, and 182 nm. The effectiveness of using higher modes to improve subsurface imaging was also shown in tapping mode AFM.^{105,106}

V. APPLICATIONS

Besides the demonstrations for subsurface imaging on well-prepared model samples,^{29,31–33,35,38} many applications have been achieved using ultrasonic AFMs for subsurface imaging in various materials and devices. This includes detecting subsurface defects in materials down to the nanoscale,^{41–43,107,108} imaging buried defects and interfaces in functional devices,^{25,29,44,109} and visualizing embedded inclusions in advanced composites⁸³ or subcellular structures in biological materials.^{36,45,110–112}

Figures 9(a) and 9(b) show UAFM images of subsurface dislocations in a HOPG sample.^{41,113} While the AFM topography in

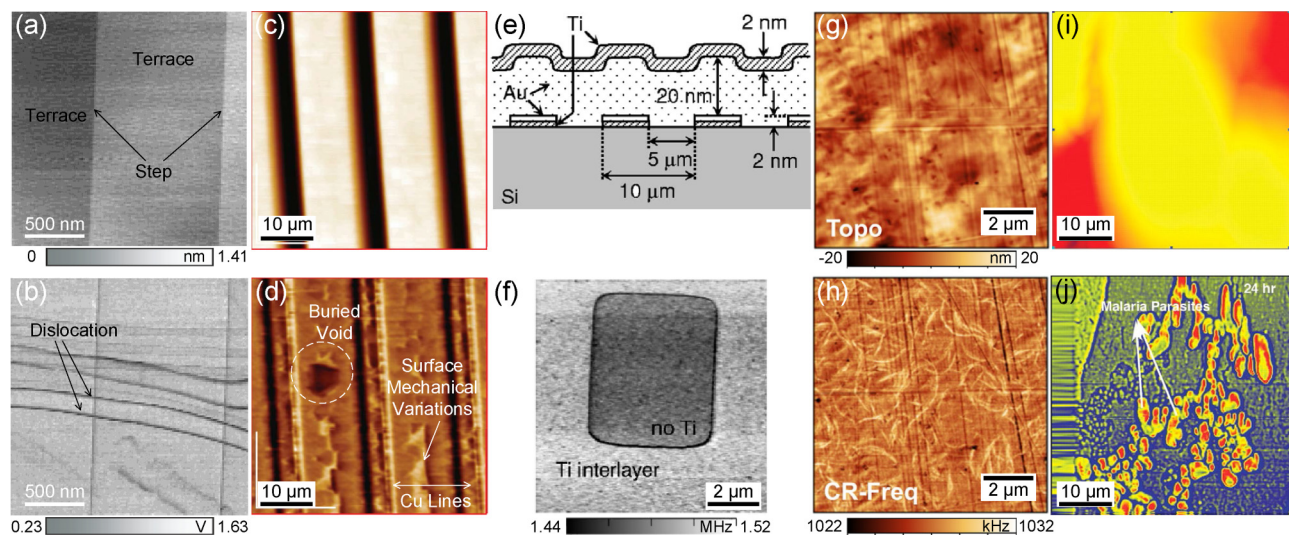


FIG. 9. (a) Topography of a cleaved HOPG surface and (b) UAFM amplitude image showing subsurface dislocations; (c) AFM topography of interconnect copper lines and (d) the corresponding SNFUH phase image showing subsurface voids; (e) cross-sectional view of Au and Ti layers adhered to a Si substrate and (f) CR frequency map showing a square indication corresponding to a region of weak adhesion; (g) topography and (h) CR frequency image of a sample containing carbon nanotube bundles in a polyimide composite; (i) topography and (j) SNFUH phase image of malaria-infected red blood cells. (a) and (b) Reproduced with permission from Tsuji and Yamanaka, Nanotechnology **12**, 301 (2001). Copyright 2001 IOP Publishing Ltd. (c) and (d) Reproduced with permission from Shekhawat *et al.*, Appl. Phys. Lett. **95**, 263101 (2009). Copyright 2009 AIP Publishing LLC. (e) and (f) Reproduced with permission from Hurley *et al.*, Appl. Phys. Lett. **89**, 021911 (2006). Copyright 2006 AIP Publishing LLC.²⁵ (g) and (h) Reproduced with permission from Cadena *et al.*, Appl. Phys. Lett. **110**, 123108 (2017). Copyright 2017 AIP Publishing LLC.³³ (i) and (j) Reproduced with permission from Shekhawat and Dravid, Science **310**, 89 (2005). Copyright 2005 American Association for the Advancement of Science.²⁹

Fig. 9(a) only shows monolayer steps and atomically flat terraces of a cleaved HOPG surface, the UAFM amplitude image in Fig. 9(b) reveals features of subsurface dislocations aligned almost parallel to each other besides the contrast from the monolayer steps on the surface. The behavior of the parallel dislocations was investigated by the authors by applying different tip loads. The results show that the dislocations move laterally with the load increasing and return to the original position as the load decreases. Such a behavior was also observed by others.¹¹⁴

Identifying defects including voids, delaminations, and cracks is important, yet challenging in integrated circuits and microelectromechanical systems. To this end, Shekhawat and co-workers demonstrated the efficacy of SNFUH in detecting subsurface defects in interconnects.^{29,44} As can be seen in Fig. 9(d), the SNFUH phase image shows indications of a buried void as well as other surface indications which are not visible in the topography image [Fig. 9(c)]. Furthermore, by using CR-AFM, adhesion maps of a buried interface as shown in Fig. 9(e) were obtained by Hurley *et al.*²⁵ From the CR frequency map [Fig. 9(f)], a square-like region of weak adhesion without a Ti adhesion layer can be clearly distinguished from other regions having the Ti interlayer. Cadena *et al.*⁸³ demonstrated the capability of CR-AFM for studying the dispersion of nanofillers in composites. Compared with the topography [Fig. 9(g)], the CR frequency image in Fig. 9(h) clearly visualized the single-walled carbon nanotube networks embedded in a polyimide matrix. Noninvasive subsurface imaging of biological materials has also been achieved using ultrasonic AFMs.^{36,45,110–112} For example, Shekhawat *et al.* have successfully imaged the internal structures including the nucleus of a mouse cell¹¹⁵ and malaria parasites inside infected red blood cells [Figs. 9(i) and 9(j)].²⁹

VI. CONCLUSION AND OUTLOOK

Ultrasonic AFMs were invented 25 years ago. Since then, they have evolved into different systems based on the cantilever's oscillatory excitation and detection schemes. Recent experimental studies support that both the real and imaginary parts of the contact stiffness, induced by subsurface features, are the key contrast origin for ultrasonic AFM in the MHz range, although the contrast mechanism of ultrasonic AFMs for subsurface imaging is not understood in all aspects. The contribution of scattering to the contrast is physically difficult to justify in the Rayleigh scattering regime, with the wavelength being several order of magnitudes larger than the subsurface feature's size.

What might lie ahead? First, realizing the quantitative reconstruction of the properties of the subsurface features is a daunting challenge. This includes determining not only the depth but also the geometry and material properties of the subsurface objects. It might be achieved by data fusion of quantitative maps with analytical models which relate the depth, the geometry, and the elastic properties of the subsurface objects.^{116,117} Such efforts have been reported in order to detect silica spheres buried in polystyrene films, using different CR frequencies,³¹ measuring the elasticity as a function of depth for a-SiOC:H patterned fins,⁸² the detection of embedded single-walled nanotubes in a polymer matrix using CR-AFM⁸³ and of cavities covered by HOPG flakes, based on a

quantitative model of the contact stiffness.⁸⁶ Furthermore, digital laminography was proposed to reconstruct subsurface objects in ultrasonic AFM images.¹¹⁸ Second, an important issue is imaging artifacts, of which topography is the most important. In case of a surface with nanoscale features such as steps, holes, bumps, and extrusions, the contact area is altered and thus the contact stiffness. This leads to variations of the cantilever contact resonance and hence to changes in the imaging parameters such as amplitude, phase, or CR frequency. To differentiate the subsurface features from topographic artifacts are important for accurate data interpretation. This may be achieved by considering the effect of topography on the contact mechanics^{119,120} and then de-convoluting its contribution. However, at present, this can only be applied to a few cases for which the contact mechanics model can be analytically established.^{119,120} For more general cases, tuning the operation frequency to reduce the sensitivity to surface structures is more applicable. This is understandable because subsurface and surface features usually correspond to different cantilever resonances, and hence, the topographic contrast can be reduced by using an operation frequency away from the resonance.^{114,121} In addition, data processing methods, including machine learning algorithms, may also be used to assist the identification of subsurface features. Finally, like other AFM methods, ultrasonic AFMs are limited by slow data acquisition, which is especially true for quantitative CR frequency and quality factor mapping. This may be eventually improved with fast data acquisition electronics and by a parallel scanning system with an array of cantilevers.

ACKNOWLEDGMENTS

C.M. acknowledges the support from the National Natural Science Foundation of China (NNSFC, No. 51675504) and the Fundamental Research Funds for the Central Universities (No. WK2090000022). W.A. thanks K. Samwer of the I. Phys. Institut at the Georg-August-Universität Göttingen for close collaboration in the course of a guest professorship starting in 2009.

DATA AVAILABILITY

Data sharing is not applicable to this article as no new data were created or analyzed in this study.

REFERENCES

- ¹W. Arnold, "Nondestructive testing of electronic and ceramic components," in *Reference Module in Materials Science and Materials Engineering*, edited by S. Hashmi (Elsevier, Oxford, 2016), pp. 1–4.
- ²U. Hartmann, *Nanostrukturforschung und Nanotechnologie*, Materialien und Systeme Vol.2 (Gruyter, Berlin, 2015).
- ³*Springer Handbook of Nanotechnology*, edited by B. Bhushan (Springer, Berlin, 2006).
- ⁴C. F. Quate, A. Atalar, and H. K. Wickramasinghe, *Proc. IEEE* **67**, 1092 (1979).
- ⁵J. Attal and C. F. Quate, *J. Acoust. Soc. Am.* **59**, 69 (1976).
- ⁶R. S. Gilmore, K. C. Tam, J. D. Young, and D. R. Howard, *Philos. Trans. R. Soc. Lond. A* **320**, 215 (1986).
- ⁷W. Dürr, D. A. Sinclair, and E. A. Ash, *Electron. Lett.* **16**, 805 (1980).
- ⁸B. T. Khuri-Yakub, C. Cinbis, C. H. Chou, and P. A. Reinholdtsen, in *Proceedings of IEEE Ultrasonics Symposium* (IEEE, Montreal, 1989), pp. 805–807.

- ⁹J. K. Zienkiewicz and A. Latuszek, in *Acoustical Imaging*, edited by H. Shimizu, N. Chubachi, and J. Kushibiki (Plenum Press, New York, 1989), pp. 219–224.
- ¹⁰K. Takata, T. Hasegawa, S. Hosaka, S. Hosoki, and T. Komoda, *Appl. Phys. Lett.* **55**, 1718 (1989).
- ¹¹K. Uozumi and K. Yamamuro, *Jpn. J. Appl. Phys.* **28**, L1297 (1989).
- ¹²B. T. Khuri-Yakub, S. Akamine, B. Hadimioglu, H. Yamada, and C. F. Quate, *Proc. SPIE* **1556**, 30–39 (1992).
- ¹³A. Moreau and J. B. Ketterson, *J. Appl. Phys.* **72**, 861 (1992).
- ¹⁴E. Chilla, W. Rohrbach, H. J. Fröhlich, R. Koch, and K. H. Rieder, *Appl. Phys. Lett.* **61**, 3107 (1992).
- ¹⁵B. Cretin and F. Sthal, *Appl. Phys. Lett.* **62**, 829 (1993).
- ¹⁶L. Robert and B. Cretin, *Surf. Interface Anal.* **27**, 568 (1999).
- ¹⁷O. Kolosov and K. Yamanaka, *Jpn. J. Appl. Phys.* **32**, L1095 (1993).
- ¹⁸K. Yamanaka, H. Ogiso, and O. Kolosov, *Appl. Phys. Lett.* **64**, 178 (1994).
- ¹⁹K. Yamanaka, H. Ogiso, and O. Kolosov, *Jpn. J. Appl. Phys.* **33**, 3197 (1994).
- ²⁰U. Rabe and W. Arnold, *Appl. Phys. Lett.* **64**, 1493 (1994).
- ²¹U. Rabe and W. Arnold, *Ann. Phys.* **506**, 589 (1994).
- ²²U. Rabe, M. Dvorak, and W. Arnold, *Thin Solid Films* **264**, 165 (1995).
- ²³U. Rabe, E. Kester, and W. Arnold, *Surf. Interface Anal.* **27**, 386 (1999).
- ²⁴K. Yamanaka, A. Noguchi, T. Tsuji, T. Koike, and T. Goto, *Surf. Interface Anal.* **27**, 600 (1999).
- ²⁵D. C. Hurley, M. Kopycinska-Mueller, E. D. Langlois, A. B. Kos, and N. Barbosa III, *Appl. Phys. Lett.* **89**, 021911 (2006).
- ²⁶P. A. Yuya, D. C. Hurley, and J. A. Turner, *J. Appl. Phys.* **104**, 074916 (2008).
- ²⁷T. Hesjedal, E. Chilla, and H. J. Fröhlich, *Appl. Phys. A* **61**, 237 (1995).
- ²⁸M. T. Cuberes, H. E. Assender, G. A. D. Briggs, and O. V. Kolosov, *J. Phys. D Appl. Phys.* **33**, 2347 (2000).
- ²⁹G. S. Shekhawat and V. P. Dravid, *Science* **310**, 89 (2005).
- ³⁰S. A. Cantrell, J. H. Cantrell, and P. T. Lillehei, *J. Appl. Phys.* **101**, 114324 (2007).
- ³¹J. P. Killgore, J. Y. Kelly, C. M. Stafford, M. J. Fasolka, and D. C. Hurley, *Nanotechnology* **22**, 175706 (2011).
- ³²K. Kimura, K. Kobayashi, K. Matsushige, and H. Yamada, *Ultramicroscopy* **133**, 41 (2013).
- ³³Z. Parlak and F. L. Degertekin, *J. Appl. Phys.* **103**, 114910 (2008).
- ³⁴A. Striegler, B. Koehler, B. Bendjus, M. Roellig, M. Kopycinska-Mueller, and N. Meyendorf, *Ultramicroscopy* **111**, 1405 (2011).
- ³⁵C. Ma, Y. Chen, W. Arnold, and J. Chu, *J. Appl. Phys.* **121**, 154301 (2017).
- ³⁶G. S. Shekhawat, A. K. Srivastava, V. P. Dravid, and O. Balogun, *ACS Nano* **11**, 6139 (2017).
- ³⁷K. Yip, T. Cui, Y. Sun, and T. Filleter, *Nanoscale* **11**, 10961 (2019).
- ³⁸S. Hu, C. Su, and W. Arnold, *J. Appl. Phys.* **109**, 084324 (2011).
- ³⁹M. H. van Es, A. Mohtashami, R. M. Thijssen, D. Piras, P. L. van Neer, and H. Sadeghian, *Ultramicroscopy* **184**, 209 (2018).
- ⁴⁰W. Wang, C. Ma, Y. Chen, L. Zheng, H. Liu, and J. Chu, *Beilstein J. Nanotech.* **10**, 1636 (2019).
- ⁴¹T. Tsuji and K. Yamanaka, *Nanotechnology* **12**, 301 (2001).
- ⁴²T. Wang, C. Ma, W. Hu, Y. Chen, and J. Chu, *Microsc. Res. Tech.* **80**, 66 (2017).
- ⁴³F. Dinelli, P. Pingue, N. D. Kay, and O. V. Kolosov, *Nanotechnology* **28**, 085706 (2017).
- ⁴⁴G. S. Shekhawat, A. Srivastava, S. Avasthy, and V. Dravid, *Appl. Phys. Lett.* **95**, 263101 (2009).
- ⁴⁵L. Tetard, A. Passian, R. H. Farahi, and T. Thundat, *Ultramicroscopy* **110**, 586 (2010).
- ⁴⁶G. S. Shekhawat, S. M. Dudek, and V. P. Dravid, *Sci. Adv.* **3**, e1701176 (2017).
- ⁴⁷O. V. Kolosov, M. R. Castell, C. D. Marsh, G. A. D. Briggs, T. I. Kamins, and R. S. Williams, *Phys. Rev. Lett.* **81**, 1046 (1998).
- ⁴⁸U. Rabe, M. Kopycinska, S. Hirsekorn, J. M. Saldana, G. A. Schneider, and W. Arnold, *J. Phys. D Appl. Phys.* **35**, 2621 (2002).
- ⁴⁹S. Banerjee, N. Gayathri, S. R. Shannigrahi, S. Dash, A. K. Tyagi, and B. Raj, *J. Phys. D Appl. Phys.* **40**, 2539 (2007).
- ⁵⁰A. Kumar, U. Rabe, and W. Arnold, *Jpn. J. Appl. Phys.* **47**, 6077 (2008).
- ⁵¹H. Wagner, D. Bedorf, S. Küchemann, M. Schwabe, B. Zhang, W. Arnold, and K. Samwer, *Nat. Mater.* **10**, 439 (2011).
- ⁵²X. Zhou, H. Miao, and F. Li, *Nanoscale* **5**, 11885 (2013).
- ⁵³Y. Luo, M. Büchsenstutz-Göbeler, W. Arnold, and K. Samwer, *New J. Phys.* **16**, 013034 (2014).
- ⁵⁴U. Rabe, K. Janser, and W. Arnold, *Rev. Sci. Instrum.* **67**, 3281 (1996).
- ⁵⁵U. Rabe, J. A. Turner, and W. Arnold, *Appl. Phys. A* **66**, S277 (1998).
- ⁵⁶U. Rabe, M. Kopycinska-Müller, and S. Hirsekorn, in *Acoustic Scanning Probe Microscopy*, edited by F. Marinello, D. Passeri, and E. Savio (Springer, Berlin, 2013), pp. 123–153.
- ⁵⁷P. A. Yuya, D. C. Hurley, and J. A. Turner, *J. Appl. Phys.* **109**, 113528 (2011).
- ⁵⁸J. P. Killgore and F. W. DelRio, *Macromolecules* **51**, 6977 (2018).
- ⁵⁹E. Kester, U. Rabe, L. Presmanes, P. Tailhades, and W. Arnold, *J. Phys. Chem. Solids* **61**, 1275 (2000).
- ⁶⁰D. C. Hurley, M. Kopycinska-Mueller, A. B. Kos, and R. H. Geiss, *Meas. Sci. Technol.* **16**, 2167 (2005).
- ⁶¹M. Kopycinska-Müller, A. Clausner, K. B. Yeap, B. Köhler, N. Kuzeyeva, S. Mahajan, T. Savage, E. Zschech, and K. J. Wolter, *Ultramicroscopy* **162**, 82 (2016).
- ⁶²J. P. Killgore, D. G. Yablon, A. H. Tsou, A. Gannepalli, P. A. Yuya, J. A. Turner, R. Proksch, and D. C. Hurley, *Langmuir* **27**, 13983 (2011).
- ⁶³D. C. Hurley, S. E. Campbell, J. P. Killgore, L. M. Cox, and Y. Ding, *Macromolecules* **46**, 9396 (2013).
- ⁶⁴M. K. Phani, A. Kumar, W. Arnold, and K. Samwer, *J. Alloy Compd.* **676**, 397 (2016).
- ⁶⁵K. Yamanaka and T. Tsuji, in *Acoustic Scanning Probe Microscopy*, edited by F. Marinello, D. Passeri, and E. Savio (Springer, Berlin, 2013), pp. 155–187.
- ⁶⁶K. Yamanaka, Y. Maruyama, T. Tsuji, and K. Nakamoto, *Appl. Phys. Lett.* **78**, 1939 (2001).
- ⁶⁷K. Kobayashi, H. Yamada, and K. Matsushige, *Surf. Interface Anal.* **33**, 89 (2002).
- ⁶⁸B. J. Rodriguez, C. Callahan, S. V. Kalinin, and R. Proksch, *Nanotechnology* **18**, 475504 (2007).
- ⁶⁹A. Gannepalli, D. G. Yablon, A. H. Tsou, and R. Proksch, *Nanotechnology* **22**, 355705 (2011).
- ⁷⁰S. Jesse, S. V. Kalinin, R. Proksch, A. P. Baddorf, and B. J. Rodriguez, *Nanotechnology* **18**, 435503 (2007).
- ⁷¹S. Jesse, R. K. Vasudevan, L. Collins, E. Strelcov, M. B. Okatan, A. Belianinov, A. P. Baddorf, R. Proksch, and S. V. Kalinin, *Annu. Rev. Phys. Chem.* **65**, 519 (2014).
- ⁷²U. Rabe, S. Hirsekorn, M. Reinstädter, T. Sulzbach, C. Lehrer, and W. Arnold, *Nanotechnology* **18**, 044008 (2007).
- ⁷³T. Tsuji, K. Kobari, S. Ide, and K. Yamanaka, *Rev. Sci. Instrum.* **78**, 103703 (2007).
- ⁷⁴X. Xu and A. Raman, *J. Appl. Phys.* **102**, 034303 (2007).
- ⁷⁵Z. Parlak, Q. Tu, and S. Zauscher, *Nanotechnology* **25**, 445703 (2014).
- ⁷⁶M. Kocun, A. Labuda, A. Gannepalli, and R. Proksch, *Rev. Sci. Instrum.* **86**, 083706 (2015).
- ⁷⁷R. Wagner and J. P. Killgore, *Appl. Phys. Lett.* **107**, 203111 (2015).
- ⁷⁸E. Dillon, K. Kjoller, and C. Prater, *Microsc. Today* **21**, 18 (2013).
- ⁷⁹R. F. Edgerton, *J. Acoust. Soc. Am.* **47**, 1229 (1970).
- ⁸⁰G. J. Verbiest, J. N. Simon, T. H. Oosterkamp, and M. J. Rost, *Nanotechnology* **23**, 145704 (2012).
- ⁸¹M. Hennes, A. M. Jakob, F. Lehnert, U. Ross, A. Lotnyk, and S. G. Mayr, *Nanoscale* **8**, 9398 (2016).
- ⁸²G. Stan, E. Mays, H. J. Yoo, and S. W. King, *Nanotechnology* **27**, 485706 (2016).
- ⁸³M. J. Cadena, Y. Chen, R. G. Reifengerger, and A. Raman, *Appl. Phys. Lett.* **110**, 123108 (2017).
- ⁸⁴G. G. Yaralioglu, F. L. Degertekin, K. B. Crozier, and C. F. Quate, *J. Appl. Phys.* **87**, 7491 (2000).
- ⁸⁵A. F. Sarioglu, A. Atalar, and F. L. Degertekin, *Appl. Phys. Lett.* **84**, 5368 (2004).

- ⁸⁶C. Ma, W. Wang, Y. Chen, W. Arnold, and J. Chu, *J. Appl. Phys.* **126**, 124302 (2019).
- ⁸⁷K. L. Johnson, *Contact Mechanics* (Cambridge University Press, Cambridge, 1985).
- ⁸⁸C. F. Ying and R. Truell, *J. Appl. Phys.* **27**, 1086 (1956).
- ⁸⁹R. Truell, C. Elbaum, and B. B. Chick, *Ultrasonic Methods in Solid State Physics* (Academic Press, New York, 1969), pp. 161–179.
- ⁹⁰G. S. Kino, *Acoustic Waves: Devices, Imaging, and Analog Signal Processing* (Prentice Hall, Englewood Cliffs, NJ, 1987), pp. 300–317.
- ⁹¹G. J. Verbiest, T. H. Oosterkamp, and M. J. Rost, *Nanotechnology* **28**, 085704 (2017).
- ⁹²G. J. Verbiest, T. H. Oosterkamp, and M. J. Rost, *Nanotechnology* **24**, 365701 (2013).
- ⁹³H. J. Sharahi, G. Shekhawat, V. Dravid, S. Park, P. Egberts, and S. Kim, *Nanoscale* **9**, 2330 (2017).
- ⁹⁴P. Maivald, H. J. Butt, S. A. C. Gould, C. B. Prater, B. Drake, J. A. Gurley, V. B. Elings, and P. K. Hansma, *Nanotechnology* **2**, 103 (1991).
- ⁹⁵M. Radmacher, R. W. Tillmann, and H. E. Gaub, *Biophys. J.* **64**, 735 (1993).
- ⁹⁶K. Kimura, K. Kobayashi, A. Yao, and H. Yamada, *Nanotechnology* **27**, 415707 (2016).
- ⁹⁷A. Yao, K. Kobayashi, S. Nosaka, K. Kimura, and H. Yamada, *Sci. Rep.* **7**, 42718 (2017).
- ⁹⁸M. Büchschütz-Göbeler, J. Rother, A. Janshoff, W. Arnold, and K. Samwer, in *Verhandl. Deutsch. Phys. Gesellschaft, Spring Meeting* (Regensburg, Germany, 2013), p. 13.5.
- ⁹⁹M. H. van Es, B. A. Quesson, A. Mohtashami, D. Piras, K. Hatakeyama, L. Fillinger, and P. L. van Neer, *arXiv:2007.01662* (2020).
- ¹⁰⁰K. B. Crozier, G. G. Yaralioglu, F. L. Degertekin, J. L. Adams, S. C. Minne, and C. F. Quate, *Appl. Phys. Lett.* **76**, 1950 (2000).
- ¹⁰¹J. A. Turner and J. S. Wiehn, *Nanotechnology* **12**, 322 (2001).
- ¹⁰²W. J. Chang, *Nanotechnology* **13**, 510 (2002).
- ¹⁰³X. Zhou, J. Fu, Y. Li, and F. Li, *J. Appl. Polym. Sci.* **131**, 39800 (2014).
- ¹⁰⁴F. J. Espinoza-Beltrán, K. Geng, J. M. Saldaña, U. Rabe, S. Hirsekorn, and W. Arnold, *New J. Phys.* **11**, 083034 (2009).
- ¹⁰⁵D. Ebeling, B. Eslami, and S. D. J. Solares, *ACS Nano* **7**, 10387 (2013).
- ¹⁰⁶A. P. Perrino, Y. K. Ryu, C. A. Amo, M. P. Morales, and R. Garcia, *Nanotechnology* **27**, 275703 (2016).
- ¹⁰⁷J. T. Zeng, K. Y. Zhao, H. R. Zeng, H. Z. Song, L. Y. Zheng, G. R. Li, and Q. R. Yin, *Appl. Phys. A* **91**, 261 (2008).
- ¹⁰⁸Q. Tu, B. Lange, Z. Parlak, J. M. J. Lopes, V. Blum, and S. Zauscher, *ACS Nano* **10**, 6491 (2016).
- ¹⁰⁹L. Muthuswami and R. E. Geer, *Appl. Phys. Lett.* **84**, 5082 (2004).
- ¹¹⁰L. Tétard, A. Passian, R. M. Lynch, B. H. Voy, G. Shekhawat, V. Dravid, and T. Thundat, *Appl. Phys. Lett.* **93**, 133113 (2008).
- ¹¹¹Y. Zhao, Q. Cheng, and M. Qian, *Chin. Phys. Lett.* **27**, 056201 (2010).
- ¹¹²M. Reggente, D. Passeri, L. Angeloni, F. A. Scaramuzza, M. Barteri, F. De Angelis, I. Persiconi, M. E. De Stefano, and M. Rossi, *Nanoscale* **9**, 5671 (2017).
- ¹¹³T. Tsuji, H. Irihama, and K. Yamanaka, *Jpn. J. Appl. Phys.* **41**, 832 (2002).
- ¹¹⁴C. Ma, Y. Chen, and W. Arnold, in *2019 IEEE International Ultrasonics Symposium* (IEEE, Glasgow, 2019), pp. 936–939.
- ¹¹⁵A. C. Diebold, *Science* **310**, 61 (2005).
- ¹¹⁶I. I. Argatov, *J. Mech. Phys. Solids* **70**, 190 (2014).
- ¹¹⁷G. Stan, S. D. Solares, B. Pittenger, N. Erina, and C. Su, *Nanoscale* **6**, 962 (2014).
- ¹¹⁸W. Arnold and A. Kulik, Patents “Ultraschallmikroskop,” German patent DE19729280C1 (5 November 1998), U.S. patent US6389885B1 (21 May 2002), Japanese patent JP2001510889A (7 August 2001), and European patent EP0995085B1 (18 September 2002).
- ¹¹⁹G. Stan and R. F. Cook, *Nanotechnology* **19**, 235701 (2008).
- ¹²⁰K. Heinze, O. Arnould, J. Y. Delenne, V. Lullien-Pellerin, M. Ramonda, and M. George, *Ultramicroscopy* **194**, 78 (2018).
- ¹²¹C. Ma, Y. Chen, and T. Wang, *AIP Adv.* **5**, 027116 (2015).